Supporting Information

Directed assembly of nanoparticle catalysts on nanowire photoelectrodes for photoelectrochemical CO_2 reduction

Authors:

Qiao Kong[1, †], Dohyung Kim[2, †], Chong Liu[1,3], Yi Yu[1], Yude Su[1], Yifan Li[1], Peidong Yang[1,2,3,4*]

Affiliations:

[1] Department of Chemistry, University of California, Berkeley, CA 94720, USA

[2] Department of Materials Science and Engineering, University of California, Berkeley, CA 94720, USA

[3] Materials Sciences Division, Lawrence Berkeley National Laboratory, Berkeley, CA 94720, USA

[4] Kavli Energy Nanosciences Institute, Berkeley, CA 94720, USA

[†] These authors contributed equally to this work.

[*] To whom correspondence should be addressed. Email: p_yang@berkeley.edu

Methods

Fabrication of the silicon nanowire array substrates. Wafer-scale silicon nanowire arrays were fabricated by deep reactive-ion etching (DRIE) method on photoresist-patterned single crystalline silicon wafers[1]. In a typical procedure, p-type boron-doped 6" Si wafer (<100> oriented, 1~5 Ohm·cm) was patterned with a dot array arranged on a square lattice with a 2 μm pitch using a standard photolithography stepper (GCA 8500). Then, this wafer underwent a low-frequency inductive-coupled plasma DRIE (STS Deep Silicon Etcher) process to produce nanowire arrays with uniform length ~22.5 μm and diameter ~850 nm. After removing the photoresist residue with O_2 plasma, ~100nm of dry thermal oxide shell was grown on the nanowires at 1050 ℃ for 100 min. 10:1 buffered hydrogen fluoride (BHF) was used to remove silicon oxide. Rinsed with H_2O (18.2 MOhm·cm resistivity) and acetone and dried under a stream of N_2 (g), the silicon nanowire arrays with diameter ~750 nm was obtained.

Fabrication of TiO_2-protected n^+p-Si PL and NW array substrates. To improve the photovoltage output[2], heavily arsenic-doped n^+ layer was formed on Si PL and NW substrate surface. A silicon handle wafer was first spin-coated with arsenic-containing spin-on dopant (SOD) (Filmtronics, Inc.) at 2200 rpm for 30 s and then baked at 150 ℃ on a hotplate for 30 min. Subsequently, Si PL and NW chips (both <100> oriented, boron-doped, 1~5 Ohm·cm) were placed upside down on the SOD-coated silicon handle wafer and subjected to rapid thermal annealing (RTA) at 900 ℃ for 3 min in N_2 atmosphere. These chips were taken out carefully from RTA chamber after cooling down under a N_2 ambient and soaked into 10:1 BHF for ~30 s to remove the thin oxide formed during n^+ doping process. After that, these chips were rinsed with H_2O (18.2 MOhm·cm resistivity) and acetone and dried under N_2 (g) stream. Finally, these n^+p-Si PL and NW chips were immediately transferred into an ALD (atomic layer deposition, Picosun ALD system) chamber. Thin TiO_2 layer (10 nm) was uniformly coated onto the surface to protect substrates from corrosion in the following photoelectrochemical measurement.

Synthesis and characterization of Au_3Cu NP. Au_3Cu NPs were synthesized via the co-reduction of both metal precursors. First, 20 mL of 1-octadecene was heated to 130°C under nitrogen atmosphere. After cooling back to room temperature, 2 mmol of oleic acid, 2 mmol of oleylamine, 0.6 mmol of gold acetate, 0.2 mmol of copper acetate and 4mmol of 1,2-hexadecanediol were added. Under the inert atmosphere, the mixture was heated to 200°C and kept at that temperature for 2 h while stirring. Afterwards, it was further heated to 280°C for 1 h. Then, the reaction was stopped by cooling it down to room temperature. Ethanol was added to the mixture to precipitate the synthesized nanoparticles and was washed once more with hexane and ethanol by centrifugation. NPs

were characterized by XRD (Bruker D8), TEM (Hitachi H-7650), UV-Vis spectroscopy (Vernier) and ICP-AES (PerkinElmer Optima 7000 DV).

Assembly of Au_3Cu NPs on Si PL and NW substrates. 90 μL of Au_3Cu NP solution was added to 210 μL hexane and sonicated for 15 s. Then, different amounts of the solution (18 μL is denoted as x1 loading with NP loading mass of 4 μg. x2 to x10 represents proportionally increased loading amounts.) were drop-casted on 0.8 cm * 0.8 cm TiO_2-protected n^+p-Si PL and NW array square pieces and dried spontaneously. Surfactant residues were removed by soaking square pieces into pure acetic acid for 90 s, followed by immersing into N, N-Dimethylmethanamide (DMF) for 1 min and subsequently into ethanol for 15 s. Finally, all Si PL and NW array square pieces with Au_3Cu NP loading were dried under N_2 stream. x2 loading was used to demonstrate photoelectrochemical reduction of CO_2.

NP coverage on NW substrates was analyzed by counting the number of particles and measuring the size of each particle in a given area using particle analysis of imageJ. Multiple measurements were performed at different regions across the substrate and NWs were sectioned into eight segments along the wire axis to perform quantitative analysis along the entire length. Theoretical estimation was obtained by assuming well-dispersed NPs on NW surface without any aggregation. Considering projected cross-sectional area of each NP to the NW surface, the theoretical coverage is represented as the ratio of the overall projected area of all NPs to the entire surface area of the NW array substrate.

Au_3Cu-n^+p-Si NW photoelectrode with ionic liquid (IL) addition. Photoelectrodes with ionic liquid (1-Butyl-3-methylimidazolium tetrafluoroborate (BMIM-BF_4)) added were prepared by following a similar way as preparing Au_3Cu-n^+p-Si NW array substrates. 0.1 μL BMIM-BF_4 was mixed with 8 mL hexanes and 10 μL of the mixture was drop-casted onto Au_3Cu-n^+p-Si NW array substrates after made.

Electrode fabrication. Photoelectrodes were fabricated on both Au_3Cu NP assembled n^+p-Si PL and NW array substrates. Ohmic contact was made by rubbing Ga-In eutectic on the back side of the square pieces. Electrical connections were made by fixing these square pieces on Ti foil with conductive silver paint and carbon tape. Finally, nail polish was used to seal the square pieces and define the active area of the photoelectrode.

Photoelectrochemical (PEC) measurements. All PEC measurements were carried out in our customized PEC setup. Two compartments of the cell are separated by an anion exchange membrane (Selemion AMV). A Pt wire was used as a counter electrode and Ag/AgCl (in 1 M KCl) as a reference electrode. Au_3Cu-n^+p-Si PL and NW electrodes were transferred inside the cell to test CO_2 reduction performance. 0.1 M $KHCO_3$

electrolyte solution was pre-electrolyzed for >16 h. Electrolyte (27.5 mL in the working compartment with gas headspace ~5 mL) was added into the cell, which was saturated with CO_2 (Praxair, 5.0 Ultra high purity) for 20 min at a flow rate of 30 mL min^{-1} under stirring. All the electrolysis was conducted under the illumination (LED light source with intensity 20 mW cm^{-2}, wavelength λ = 740 nm, calibrated with a standard Si photodiode) at room temperature and 1 atm CO_2 with electrolyte pH at 6.8. Each measurement was conducted multiple times to check the consistency of our experiments. Electrochemical data presented in this work are the average values out of these multiple measurements and error bars are one times the standard deviation.

During chronoamperometry, effluent gas from the cell went through the sampling loop of a gas chromatograph (SRI) to analyze the concentration of gas products. The gas chromatograph was equipped with a molecular sieve 13X and hayesep D column with Ar (Praxair, 5.0 Ultra high purity) flowing as a carrier gas. The separated gas products were analyzed by a thermal conductivity detector (for H_2) and a flame ionization detector (for CO). Quantification of the products was performed with the conversion factor derived from the standard calibration gases. To avoid any issues related to gas product detection, such as large fluctuations in the total amount being observed at each measurement point and detection efficiency varying with the total amount of current being generated, faradaic efficiencies of the products were normalized with the sum being unity.

Liquid products were analyzed afterwards by qNMR (Bruker AV-500) using dimethyl sulfoxide as an internal standard. Solvent presaturation technique was implemented to suppress the water peak. Faradaic efficiencies were calculated from the amount of charge passed to produce each product divided by the total charge passed at a specific time or during the overall run.

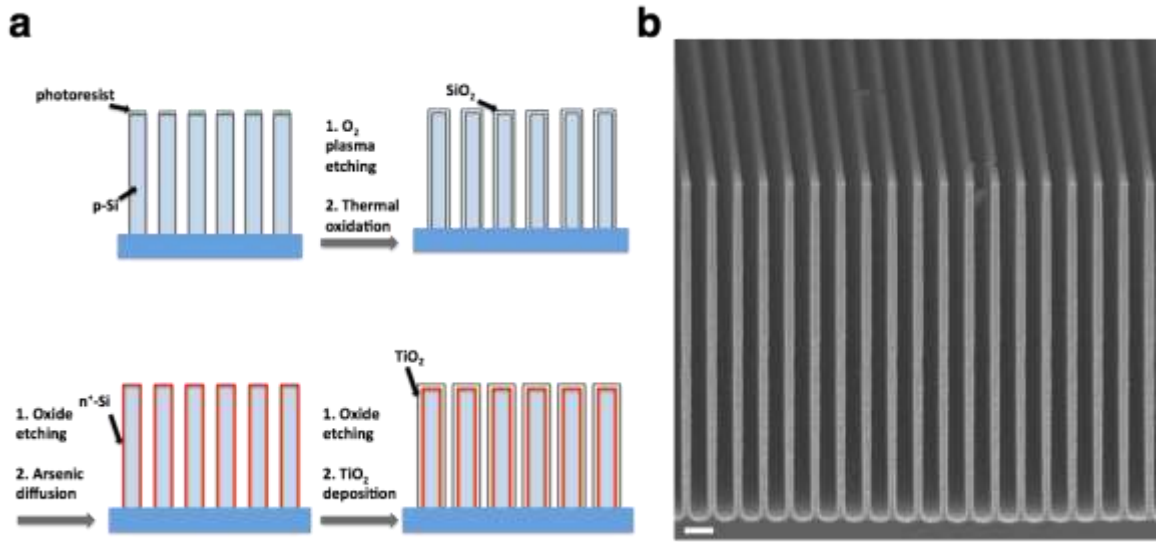

Figure S1 Fabrication of TiO_2-protected n^+p-Si NW array device. (a) Schematic of Si NW array device fabrication process. (b) SEM image of TiO_2-protected n^+p-Si NW array substrate. Scale bar is 2 μm.

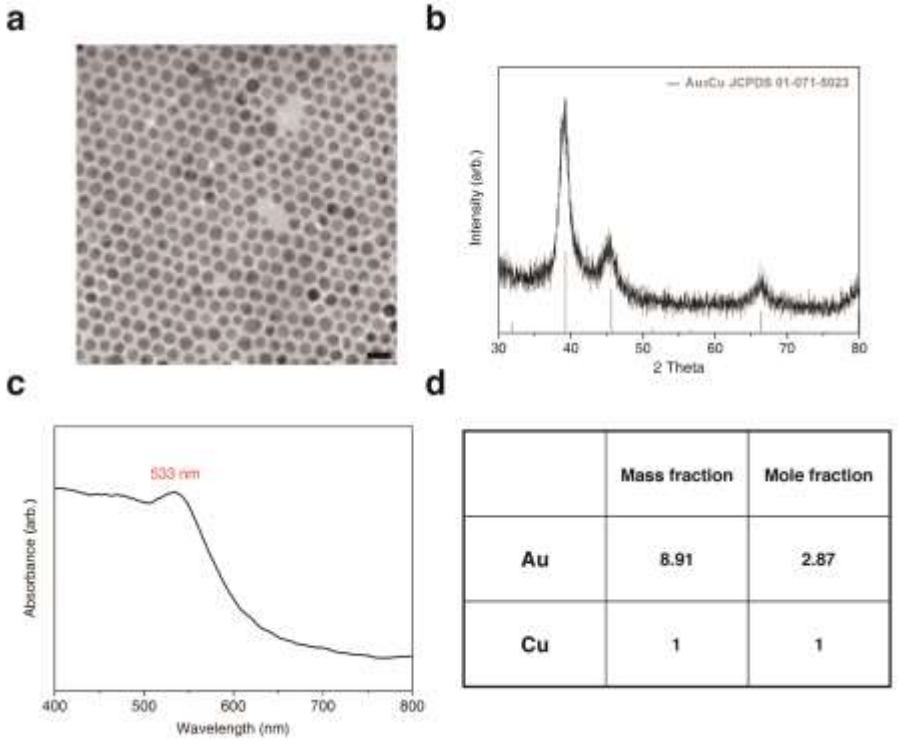

	Mass fraction	Mole fraction
Au	8.91	2.87
Cu	1	1

Figure S2 Characterization of Au_3Cu nanoparticles. (a) TEM image of Au_3Cu nanoparticles. Average size is 10.8±1.2 nm. Scale bar is 20 nm. (b) XRD patterns of Au_3Cu nanoparticles compared with diffraction patterns from the database (Au_3Cu, JCPDS 01-071-5023). (c) Ultraviolet-visible absorption spectra of Au_3Cu nanoparticles.

Surface plasmon resonance peak of Au_3Cu is around 533 nm. (d) ICP-AES data with the mass and atomic fraction of Au and Cu.

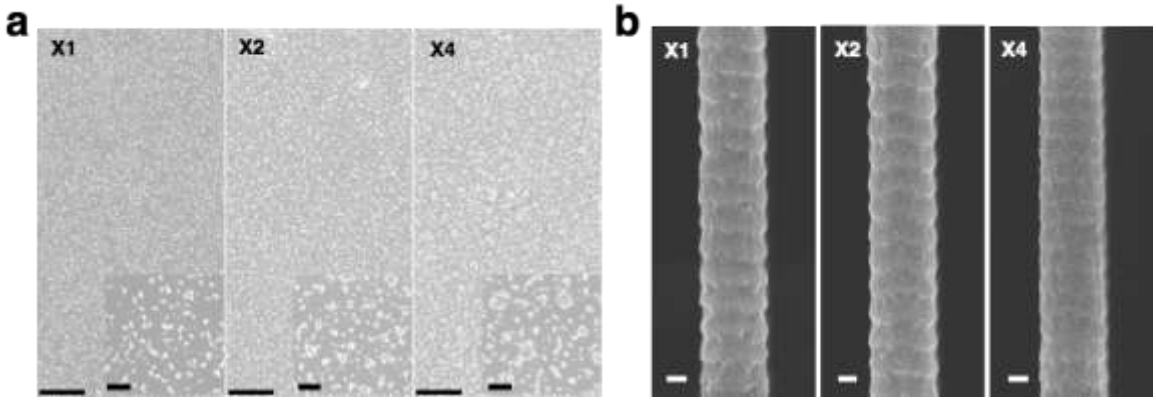

Figure S3 Au_3Cu NP assembly on PL and NW substrates. Representative SEM images of Au_3Cu NPs assembled Si PL (a) and NW (b) substrates with different loading amounts that have been proportionally varied. The absolute loading amounts were identical to both substrates and x1 loading refers to NP mass of 4 μg. Scale bar in (a) is 1μm and for inset 200 nm. Scale bar in (b) is 200 nm.

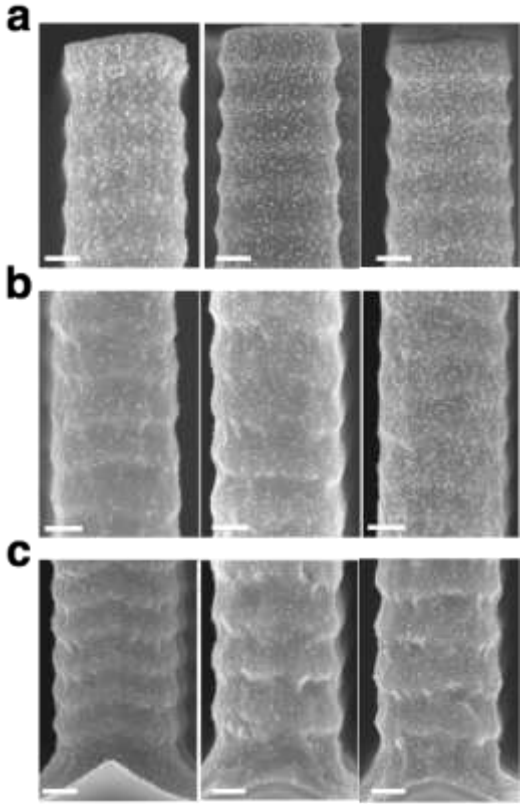

Figure S4 Representative SEM images of x1 (left column), x2 (middle column) and x4 (right column) loading of Au_3Cu NP assembly on Si NW array substrate from top to bottom. Top segment (a) had a relatively higher NP coverage compared to the middle (b) and the bottom (c). Scale bar is 200 nm. The images shown in (b) are a good representation of the 3/4 of the wire. Top and bottom segments are the rest 1/8 of the overall length, respectively.

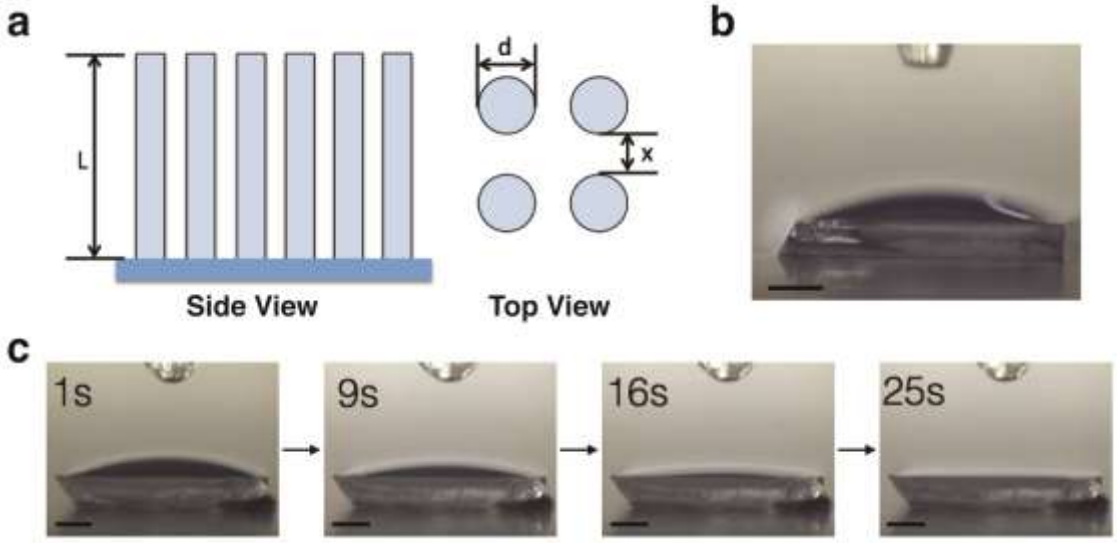

Figure S5 Wetting and drying of NP solution on NW substrate. (a) Illustration of the nanowire substrate. (b) NP solution droplet on Si PL substrate. Solution wetting indicates that the interfacial energy of solid/liquid (γ_{SL}) is lower than that of solid/vapor (γ_{SV}), according to Young's equation. (c) Images of NP solution droplet drying on Si NW substrate. As the liquid advances into the pillar patterns, the energy change $\Delta E = \frac{\pi dy}{(x+d)^2}(\gamma_{SL} - \gamma_{SV})$,[3] where y denotes the penetration depth of the liquid from the top of the pillars, is negative. This implies that vertical penetration of the solution into grooves between the wires may happen instantaneously to reach Wenzel state where the solution wets the entire substrate and is in intimate contact with solid asperities. Then the solution evaporates down to the level of the NWs, concentrating NPs at the top of wires. Eventually, assisted by the NW morphology, the solution dries in the vertical direction along the wires with the NPs being deposited[4,5]. The particles are held to the substrate while the liquid front moves along the wires. This unidirectional drying process allows NPs to be well dispersed along the walls with a coverage gradient from top to bottom. Scale bar 1 mm.

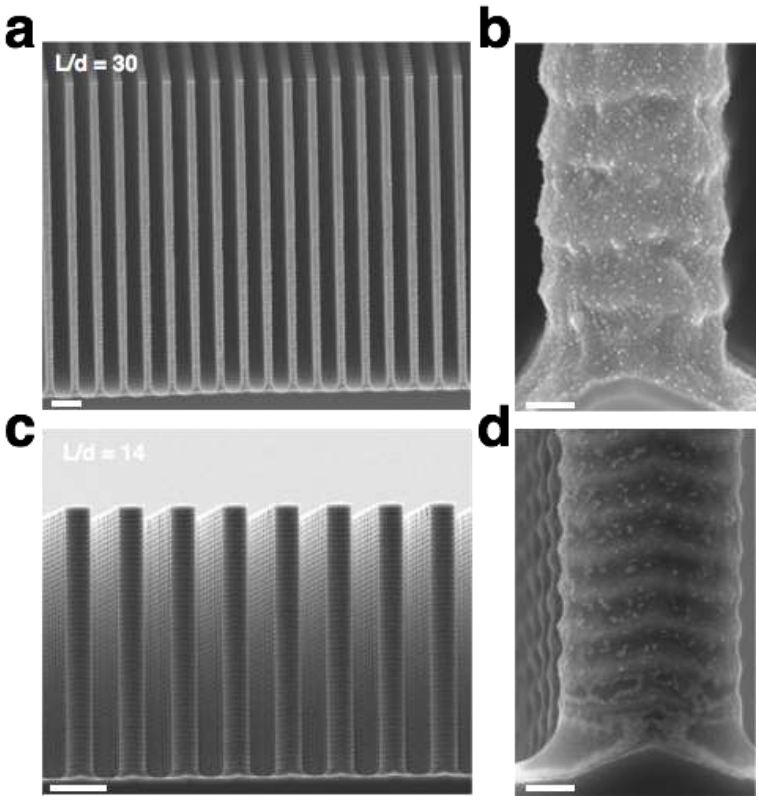

Figure S6 Effect of the NW aspect ratio on NP assembly. SEM images of Si NW arrays with high (a) and low (c) aspect ratio (the ratio of length (L) to diameter (d)). In this case, length (L) is the only variable while the diameter (d) is kept the same. Scale bar is 2 μm. The provided surface area for NPs on both substrates with different aspect ratios was comparable (identical to keeping the theoretical coverage similar) to ensure that NWs can provide sufficient area for NP assembly. Assembly procedures were identical, using the NP solution with the same concentration but varying the amount drop-casted depending on the real surface area. Difference in the NP assembly was observed at the bottom of each substrate. In contrast to what was observed on the Si NWs with higher aspect ratio (b), large amount of NPs aggregated and settled at the base of the substrate with lower aspect ratio (d). Scale bar of (b) and (d) is 200 nm.

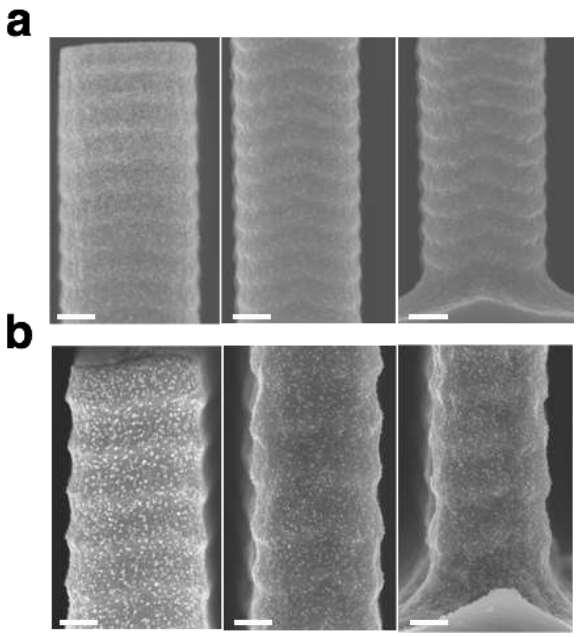

Figure S7 SEM images of Au_3Cu NP assembly on Si NW array substrate from top (left) to bottom (right) when ligand amount is varied. (a) Less ligand containing Au_3Cu NP solution drop-casted onto Si NW array. (b) More ligand containing Au_3Cu NP solution drop-casted onto Si NW array. The ligand amount is controlled by adding more washing steps or adding additional ligands without disturbing NP dispersion in solution. By washing the NPs more, we clearly evidenced clustering and increased coverage at the top of the NWs, which indicated that strong interaction with the support that may have resulted from depriving the surface ligands did not allow the NPs to reach the bottom. However, if additional surface ligands were present, we found more NPs to reach the base of the substrate. Scale bar is 200 nm.

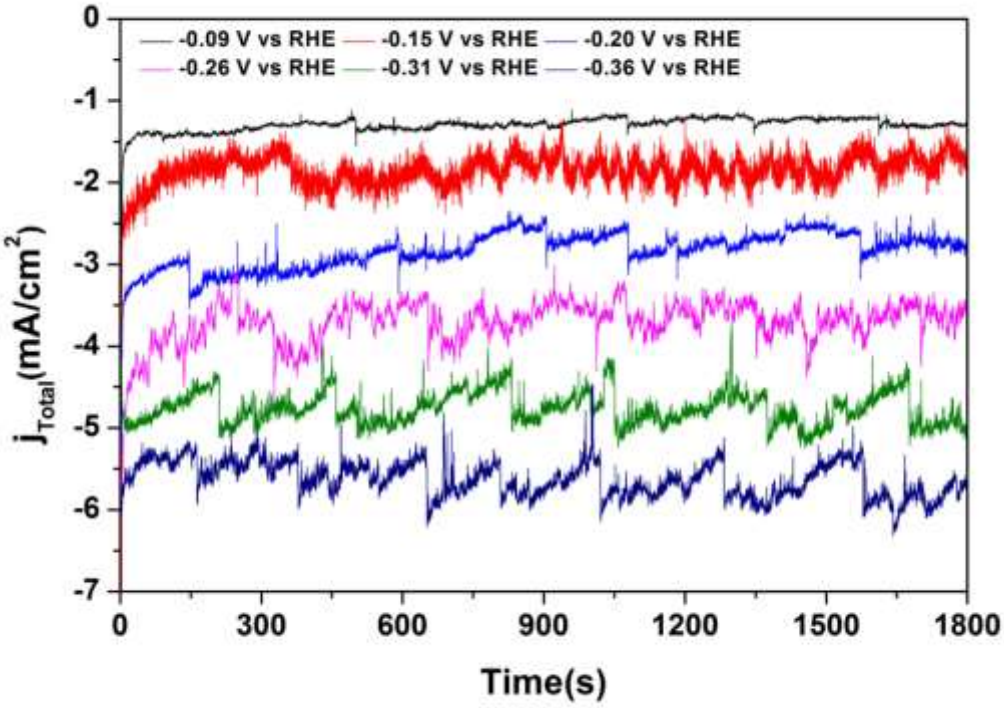

Figure S8 CO_2 reduction activity (total current density) as a function of time at various potentials for Au_3Cu-n^+p-Si NW array photoelectrode under illumination. Current fluctuates more with more negative potential applied due to the vigorous gas formation, which blocks the active area on the electrodes. In general, current showed negligible change over time indicating that product turnover is maintained under all potential conditions. In addition, faradaic efficiency is rather consistent during this time period, meaning the distribution of products stays relatively stable.

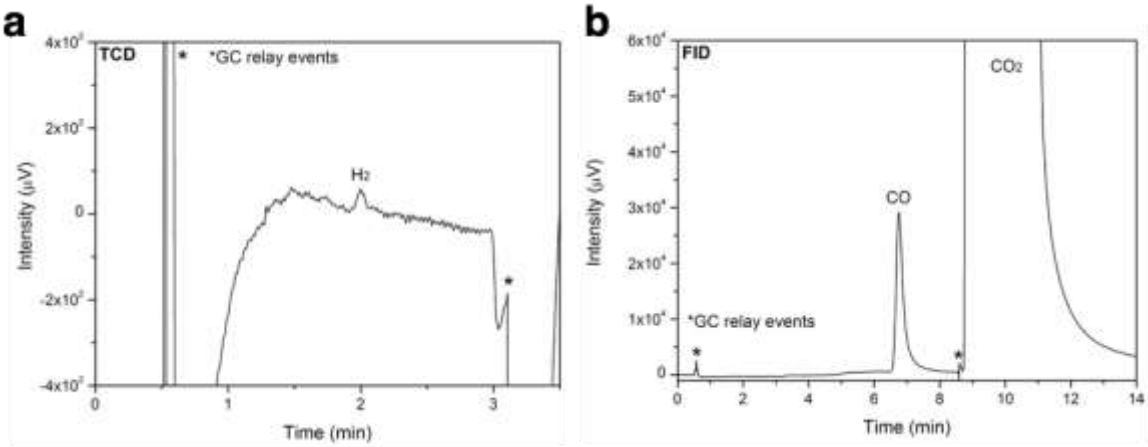

Figure S9 Gas chromatography spectrum of major products CO and H_2. H_2 was detected with TCD detector (a) while CO with FID detector (b). Quantitative analysis of CO:H_2 ratio was calculated showing CO was the dominant product.

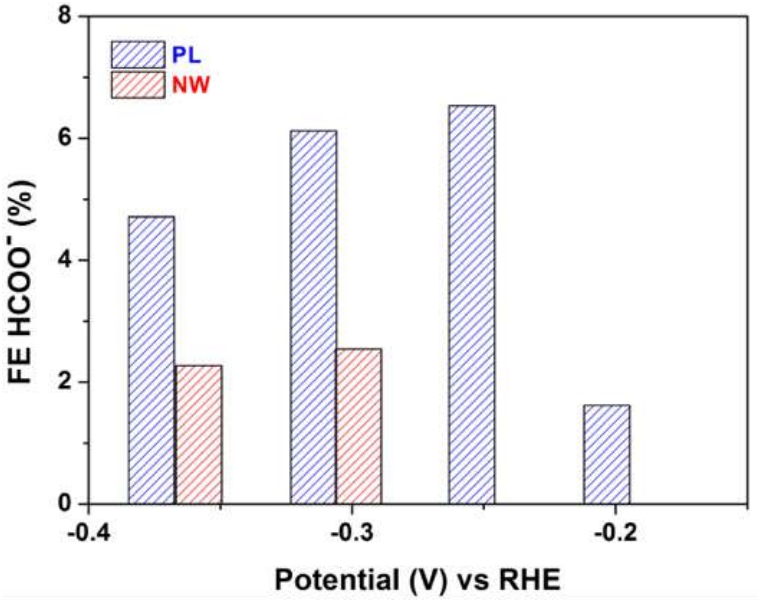

Figure S10 Comparison of formate production on Au_3Cu NP integrated Si PL and NW substrates under illumination.

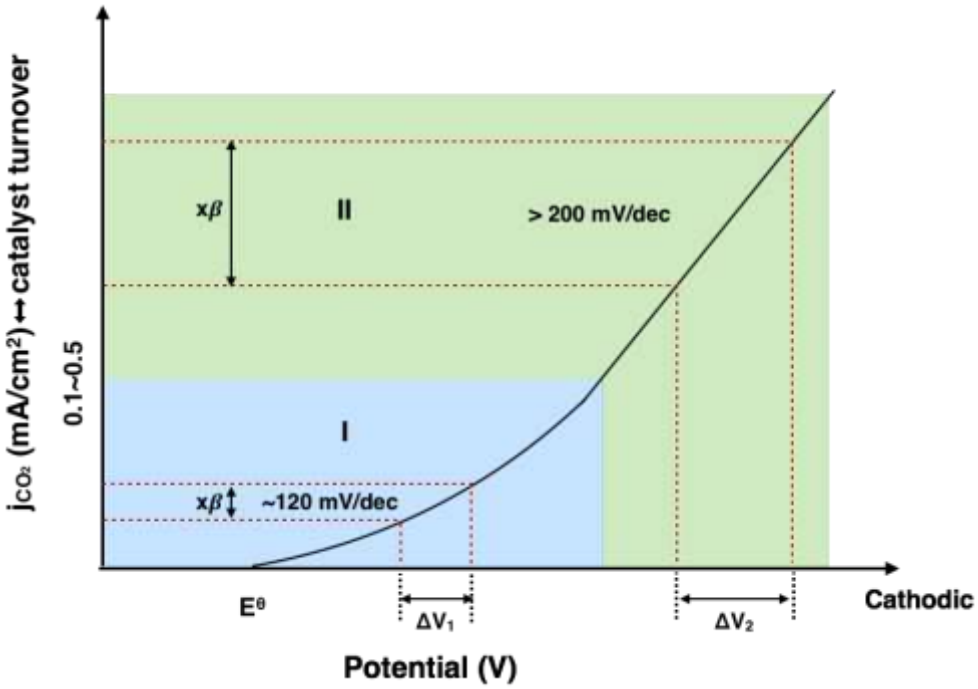

Figure S11 Schematic profile of current density for reducing CO_2 with applied potentials. In the operational current density region of interest (region II, 1 mA/cm^2 ~ 10 mA/cm^2), the overpotential that needs to be added to drive the reaction further is higher compared with that in the region where catalytic activity is dominated by one-electron rate-determining step in forming the intermediate CO_2^- (region I with Tafel slope around 120mV/dec). This is due to CO_2 mass transport limitation and mechanistic pathway shift favoring hydrogen evolution at negative bias. With a certain factor (β) of electron flux dilution leading to a relaxed catalyst turnover, the overpotential being lowered in region II is greater ($\Delta V_2 > \Delta V_1$) indicating that NW photoelectrode would be more advantageous for driving CO_2 reduction reaction at a reduced bias in the practical regions of current output.

References

(1) Liu, C.; Tang, J.; Chen, H. M.; Liu, B.; Yang, P. *Nano Lett.* **2013,** *13,* 2989–2992.

(2) Warren, E. L.; Boettcher, S. W.; Walter, M. G.; Atwater, H. A.; Lewis, N. S. *J. Phys. Chem. C* **2011,** *115,* 594–598.

(3) Murakami, D.; Jinnai, H.; Takahara, A. *Langmuir* **2014,** *30,* 2061–2067.

(4) Chi, L. F.; Gleiche, M.; Fuchs, H. *Nature* **2000,** *403,* 173–175.

(5) Huang, J.; Kim, F.; Tao, A. R.; Connor, S.; Yang, P. *Nat. Mater.* **2005,** *4,* 896–900.